Microfluidic synthesis of dye-loaded polycaprolactone-*block*-poly(ethylene oxide) nanoparticles: Insights into flow-directed loading and *in vitro* release for drug delivery

Aman Bains, Jeremy E. Wulff, & Matthew G. Moffitt

August 2016

Microfluidic Synthesis of Dye-Loaded Polycaprolactone-block-poly(ethylene oxide) Nanoparticles: Insights into Flow-Directed Loading and *In Vitro* Release for Drug Delivery

Aman Bains, Jeremy E. Wulff, and Matthew G. Moffitt*

Department of Chemistry, University of Victoria, P.O. Box 3065, Victoria, BC, Canada V8W 3V6

Keywords: Block Copolymers, Self-Assembly, Drug Delivery, Microfluidics, Nanoparticles

ABSTRACT: Using the fluorescent probe dye 1,1′-dioctadecyl-3,3,3′,3′-tetramethylindocarbocyanine perchlorate (DiI) as a surrogate for hydrophobic drugs, we investigate the effects of water content and on-chip flow rate on the multiscale structure, loading and release properties of DiI-loaded poly(ε-caprolactone)-*block*-poly(ethylene oxide) (PCL-*b*-PEO) nanoparticles produced in a gas-liquid segmented microfluidic device. We find a linear increase in PCL crystallinity within the nanoparticle cores with increasing flow rate, while mean nanoparticle sizes first decrease and then increase with flow rate coincident with the disappearance and reappearance of long filament nanoparticles. Loading efficiencies at the lower water content (cwc + 10 wt %) are generally higher (up to 94%) compared to loading efficiencies (up to 53%) at the higher water content (cwc + 75 wt %). In vitro release times range between ~2-4 days for nanoparticles produced at cwc + 10 wt % and >15 days for nanoparticles produced at cwc + 75 wt %. At the lower water content, slower release of DiI is found for nanoparticles produced at higher flow rate, while at high water content, release times first decrease and then increase with flow rate. Finally, we investigate the effects of the chemical and physical characteristics of the release medium on the kinetics of in vitro DiI release and nanoparticle degradation. This work demonstrates the general utility of dye-loaded nanoparticles as model systems for screening chemical and flow conditions for producing drug delivery formulations within microfluidic devices.

KEYWORDS: Block Copolymers, Polymer Nanopaticles, Micelles, Drug Delivery, Microfluidics.

INTRODUCTION

Block copolymer-based drug delivery nanoparticles have a number of potential advantages over more conventional lipid-based systems, including increased morphological variability, robustness, and ease of functionalization.[1-4] In aqueous media, amphiphilic block copolymers form micellar nanoparticles of various morphologies, including nanoscale spheres, cylinders (filomicelles), lamellae, and vesicles (polymersomes), consisting of cores of aggregated hydrophobic blocks capable of solubilizing lipophilic drug molecules, surrounded by a soluble coronal layer of hydrophilic blocks.[5-11] Biocompatible and semicrystalline block copolymers, such poly(L-lactide)-*block*-poly(ethylene oxide) (PLLA-*b*-PEO)[12-15] and poly(ε-caprolactone)-*block*-poly(ethylene oxide) (PCL-*b*-PEO)[7,16-20] are often applied to drug delivery applications. Such materials self-assemble to form nanoparticles with structural hierarchy or multiscale organization, due to a combination of features at the colloidal length scale (~10-100 nm; e.g. nanoparticle size and morphology) and at the nanoscale (~1-10 nm; e.g. crystallization of hydrophobic segments within nanoparticle cores). For drug delivery applications, structural features on both disparate length scales strongly affect the function of block copolymer nanocarriers.[21,22,19,23-25] For example, at the colloidal scale, the sizes of nanoparticles carrying anticancer agents will influence their localization within tumours *via* the enhanced permeability and retention effect (EPR),[26] whereas nanoparticle morphologies have been shown to significantly affect *in vivo* circulation times:[21,22,19,23,25] at the nanoscale, the internal crystallinity of semicrystalline nanoparticles is an important factor in such important figures of merit as stability, flexibility, and release kinetics.[21,22,19,23-25] These examples highlight a critical need for controlling all levels of multiscale structure in order to obtain hierarchical nanoparticles with the desired physical, chemical,

and biochemical properties for a specific therapeutic application.

Our group has recently developed a microfluidic platform consisting of a segmented gas-liquid microreactor for the generation of block copolymer nanoparticles offering continuous variability of structure *via* the convenient "top-down" variable of on-chip flow rate.[27-30,20] For the amorphous block copolymer polystyrene-*block*-poly(acrylic acid), PS-*b*-PAA, we showed that flow-directed self-assembly enables control over the sizes and morphologies of the resulting nanoparticles as a result of shear effects on particle coalescence and breakup.[27,28,30] More recently, we demonstrated that for the semicrystalline copolymer PCL-*b*-PEO, flow rate provides a top-down experimental handle on structure at *both* critical length scales, including nanoparticle size, morphology, *and* internal crystallinity;[20] we further showed that such multiscale structure control allows the function of drug delivery nanoparticles, in particular release rates of the encapsulated drug paclitaxel (PAX), to be tuned via flow rate.[20] In addition, it was found that at a given flow rate the on-chip chemical environment (i.e. water content) also strongly influences the structural products of self-assembly and the function of the resulting nanoparticles (i.e. PAX loading efficiencies and release rates).[20] In order to develop this microfluidic reactor as a general platform for the controlled manufacturing of polymeric drug delivery nanoparticles, we consider that each hydrophobic drug will interact differently with the solvent and polymer environments, thus affecting self-assembly and loading in different ways.[31-35] Optimal on-chip chemical and flow conditions will therefore need to be tailored for specific drug cargos, requiring an increased understanding of the effects of flow rate on nanoparticle structure and function under a wide range of on-chip chemical conditions (e.g. solvent, water content, polymer concentration, drug-to-polymer ratio).

Fluorescent dyes are often used as model hydrophobic probes or "drug surrogates" for the development of block copolymer- and lipid-based nanocarriers.[31-35,29] Although the refinement of on-chip conditions for a given application will inevitably require experimentation with the specific target drug, initial investigations using a hydrophobic probe with a size and solubility representative of a range of hydrophobic drugs can provide insight into general trends and establish important *a priori* information for subsequent studies. This approach increases both the time and cost efficiency of formulation development, as model probes are available at a fraction of the cost of some therapeutics identified for drug delivery applications. In addition, the high sensitivity of fluorescence measurements allows probe dyes to be quantified from much smaller sample aliquots than are required for non-fluorescent drug molecules (including PAX). This makes probe dyes particularly well suited for the investigation of microfluidic systems, where continuous variability of flow and chemical parameters allows a large number of small-volume samples to be collected within a short timeframe.

For example, we recently utilized the dyes pyrene and naphthalene as model probes with high and low chemical affinities, respectively, for the PS cores of PS-*b*-PAA nanoparticles formed in a segmented gas-liquid microfluidic reactor under various chemical conditions and two different on-chip flow rates (5 and 50 μL/min).[29] In that study, it was shown that loading efficiencies first increased and then decreased with increasing water content at a constant flow rate as a result of competing thermodynamic and kinetic factors. It was also found that the effect of flow rate on dye loading was generally small, except at an intermediate water content where a higher particle aggregation number at the lower flow rate corresponded to a higher loading efficiency. Maximum on-chip loading efficiencies measured for the pyrene and naphthalene probes were ~73 % and ~11% respectively, reflecting the higher solubility of the former molecule in the PS cores of the nanoparticles. For nanoparticles prepared at the intermediate water content and at two different flow rates, *in vitro* release kinetics of the pyrene probe were compared, revealing that greater burst release followed by longer overall release times were associated with nanoparticles formed at the higher flow rate.

Compared to amorphous nanoparticles such as PS-*b*-PAA, the structural hierarchy of semicrystalline PCL-*b*-PEO nanoparticles should give rise to even more complex flow effects on the loading and release of hydrophobic molecules, due to the interplay of flow-induced structure formation processes operating on multiple length scales, including particle coalescence, particle breakup, and crystallization within particle cores. This is supported by our preliminary loading and release data for the specific drug PAX in PCL-*b*-PEO nanoparticles formed on-chip at three different flow rates and at a single water content, which suggest that flow-directed particle size, internal crystallinity, and mixing all influence loading and release of PAX from the nanocarriers.[20] An appropriate dye with high affinity for PCL should enable studies providing a greater understanding of flow effects on loading efficiencies for various hydrophobic drugs under a broad range of chemical conditions.

A specific characteristic of drug delivery nanoparticles that is widely studied is the *in vitro* release of the encapsulated drug into an aqueous reservoir.[36,37,33,38,39,34,40-50,29,20] Although the chemical and physical characteristics of the reservoir are often set to mimic physiological conditions, it has been shown that *in vitro* experiments fall short of recreating the dynamic release mechanisms that exist *in vivo*, such that *in vitro* and *in vivo* release kinetics are often drastically different.[51,18,19] Nonetheless, the ease of carrying out *in vitro* experiments compared to the financial and practical challenges of *in vivo* testing make the former an important tool in the development of chemistry and methods for nanocarrier formulations, providing a baseline and point of comparison for more advanced testing. The comparison of *in vitro* results from different studies is often complicated by the range of different experimental conditions that are applied. For example, Eisenberg and

others have described *in vitro* release of hydrophobic molecules into a medium of running tap water in a setup designed to maintain a constant chemical potential gradient under "perfect sink" conditions.[34] Other studies have instead mimicked perfect sink conditions using a large volume differential (≥ 250×) between the release medium and the sample. Within the latter group, the release medium can vary from pure (deionized) water,[37,34,29] to phosphate buffered saline (PBS),[36,38,40,43] to PBS containing dissolved albumin,[1,39,42,44,46] to cell lysate,[52,53] representing increasing similarity with the chemical complexity of physiological environments. An additional complication is the demonstrated effect of temperature and pH on the *in vitro* hydrolytic breakdown of PCL and similar degradable polymers which provides an additional mechanism for release.[54,55] To our knowledge, a systematic comparison of *in vitro* release kinetics into a variety of release media, representing a wide range of physical and chemical characteristics, has not yet appeared in the literature. Such a study should prove immensely useful for establishing which experimental features of *in vitro* release have the strongest influence on the release kinetics of polymeric nanocarriers.

In this paper, we apply the hydrophobic dye 1,1′-dioctadecyl-3,3,3′,3′-tetramethylindocarbocyanine perchlorate (DiI) as a fluorescent probe to study on-chip loading into PCL-*b*-PEO nanocarriers under various chemical and flow conditions within a segmented gas-liquid microfluidic reactor, followed by *in vitro* release from the resulting nanoparticle formulations. DiI is a well-known biological probe commonly applied to labeling cells and tissues,[56,57] and has been shown to have a high affinity for the PCL cores of PCL-*b*-PEO nanoparticles in aqueous and polar mixed solvent media.[34,35] The results of this study provide important insights into the effects of on-chip flow rate and water content on loading efficiencies and release kinetics of nanocarriers synthesized in our segmented microfluidic reactor, while also developing a general strategy for establishing process-structure-function relations for nanocarriers manufactured using microfluidics. Furthermore, we describe a systematic study of the dependence of nanoparticle degradation and *in vitro* release of hydrophobic probe on the chemical and physical characteristics of the release medium, comparing effects of temperature, static medium vs. constant flow, and various release media including PBS buffer, albumin solution, and cell lysate.

EXPERIMENTAL

Materials. Poly(caprolactone)-*block*-poly(ethylene oxide) (PCL_{105}-*b*-PEO_{114}, where numbers in subscripts denote number-average degrees of polymerization for the respective blocks) was purchased from Advanced Polymer Inc. and used as received. *N*,*N*-Dimethylformamide (DMF) (Aldrich, 99.9+%, HPLC grade, H_2O < 0.03%) was used as received without further purification. 1,1′-Dioctadecyl-3,3,3′,3′-tetramethylindocarbocyanine perchlorate (DiI) (Aldrich) was used as received. The Bio-Rad protein assay (Bradford assay) was used as received without further modifications. All quantitative stock solutions of PCL-*b*-PEO/DiI in DMF were prepared gravimetrically by accurately weighing the solids into a glass vial followed by gravimetric addition of a known quantity of DMF; stock solutions were then equilibrated overnight with stirring before further use. All experiments, unless otherwise noted, were run in triplicate from separately prepared stock solutions.

Critical Water Content Determination. Static light scattering (SLS) measurements were carried out to accurately determine the critical water content (cwc) of 0.33 wt % DMF solutions of PCL-*b*-PEO, which was the initial condition for all self-assembly experiments in this study. The cwc is the minimum concentration of water required to induce spontaneous self-assembly of amphiphilic block copolymers, dissolved in a good solvent, into micellar aggregates. SLS measurements were carried out using a Brookhaven Instruments photon correlation spectrometer equipped with a BI-200SM goniometer, a BI-9000AT digital autocorrelator, and a Melles Griot He-Ne Laser (633 nm) with a maximum power output of 75 mW.

A 1.0 wt % stock solution of PCL-*b*-PEO in DMF was filtered through a Teflon syringe membrane filter with a nominal pore size of 0.45 μm (VWR) into precleaned scintillation vials. The filtered stock was then diluted to 0.33 wt % by gravimetric addition of the required quantity of DMF. To the resulting ~6 g of solution, deionized water was added in successive 0.03-0.06 g quantities via a microsyringe equipped with two membrane filters (VWR) with nominal pore size of 0.20 μm connected in series. After each addition of water, the solution was agitated using a vortexer to aid in mixing. The solution was then allowed to equilibrate for 15 min before measuring the scattered light intensity. All measurements were carried out at a scattering angle of 90° and a temperature of 23 °C. From the resulting plot of scattered light intensity versus weight percentage of added water (Figure S1), the cwc was determined from the intercept of linear fits to the baseline and the region of the plot in which scattered light intensity increased sharply (above the cwc). Determinations of cwc were carried out three times from the same stock solution and the mean value and standard deviation of the three measurements were used to calculate the reported cwc and experimental error: cwc = 5.5 ± 0.4 wt %.

Microfluidic Chip Fabrication. Negative masters were fabricated on high quality silicon wafers (Silicon Quest International, Santa Clara, CA) using the negative photoresist SU-8 100 (Microchem Inc.). Immediately prior to use, the wafers were heated on a hot plate at 200 °C for 20 minutes to remove moisture. A 150 μm-thick SU-8 film was spin-coated onto the silicon and then heated to 95 °C for 60 minutes to remove residual SU-8 solvent. A photomask was then placed over the SU-8 film and exposed to UV light for 180 s. Then, the UV-treated film was heated at 95 °C for 20 min before submersion in SU-8 developer (Microchem) until all unexposed photoresist was removed.

Microfluidics chips were fabricated from poly(dimethylsiloxane) (PDMS) using a SYLGARD 184 silicon elastomer kit (Dow Corning, Midland, MI). For chips used in the preparation of nanoparticles without PAX, an elastomer base-to-curing agent ratio of 10:1 was employed as recommended by the kit. However, improved adhesion between the channel and substrate PDMS layers was later found when base-to-curing agent ratios were adjusted to 7:1 and 20:1 for the two layers, respectively, and these ratios were employed for the PAX-encapsulation experiments described the text. For fabrication of all PDMS chips, the elastomer and curing agent were mixed together and degassed in a vacuum chamber. The degassed PDMS was then poured over the negative master in a Petri dish and further degassed until all remaining air bubbles were removed. The PDMS was then heated at 85 °C for ~60 min until cured. The microfluidic chip was then peeled off of the negative master and holes were punched through its reservoirs to allow for the insertion of tubing. A thin PDMS film (substrate layer) was also formed on a glass slide by spin-coating and was permanently bonded to the base of the microfluidic reactor (channel layer) after both components were exposed to oxygen plasma for 60 s. The reactor has a set channel depth of 150 μm and consists of a sinusoidal mixing channel 100 μm wide and 100 mm in length and a sinusoidal processing channel 200 μm wide and 740 mm in length.

For further stabilization of the bubble generation process, an external resistor chip was used between the Ar gas tank and the microfluidic chip. The resistor chips served as high pressure drop systems to efficiently dampen the pressure fluctuations caused by the Ar gas tank and the bubble generation process. The total pressure drop in the external resistor chip was at least one order of magnitude higher than the pressure drop in the reaction channel. The resistor chip channels were 1000 mm long, 150 μm deep and 400 μm wide.

Flow Delivery and Control. Pressure-driven flow of liquids to the reactor inlet was provided using 1 mL gas-tight syringes (Hamilton, Reno, NV) mounted on syringe pumps (Harvard Apparatus, Holliston, MA). The microchip was connected to the liquid syringes via 1/16th-inch (OD) Teflon tubing (Scientific Products and Equipment, ON). Gas flow was introduced to the microchip via an Ar tank regulator and a downstream regulator (Johnston Controls) for fine adjustments. The microchip was connected to the downstream regulator through a 1/16th-inch (OD) / 100-μm (ID) Teflon tube (Upchurch Scientific, Oak Harbor, WA). The liquid flow rate (Q_{liq}) was programmed via the syringe pumps and the gas flow rate (Q_{gas}) was fine-tuned via the downstream pressure regulator in order to dial in the nominal total flow rates described in the main text. Due to the compressible nature of the gas and the high gas/liquid interfacial tension, discrepancies arise between the nominal (programmed) and actual values of Q_{gas}, Q_{gas}/Q_{liq}, and the total flow rate (Q_{total}). Therefore, actual gas flow rates were calculated from the frequency of bubble formation and the average volume of gas bubbles, determined from image analysis of the mean lengths of liquid and gas plugs, L_{liq} and L_{gas}, respectively, under a given set of flow conditions. This method of flow calculation has been previously employed in the context of gas-liquid segmented flow in the microfluidic device.[27] Actual flow parameters pertaining to each microfluidic experiment described in the paper are listed in Table S1. For all experiments, the relative gas-to-liquid flow ratio, Q_{gas}/Q_{liq} ~1 and all actual Q_{total} values are within 10% of nominal values reported in the main text.

Visualization of the gas bubbles and liquid plugs within the microfluidic reactor was achieved using an upright optical microscope (Omax) with a 10x-objective lens. Images were captured using a 2.07 megapixel PupilCam (Ken-A-Vision) and mean lengths of liquid and gas plugs were determined from the images using image analysis software (ImageJ).

Microfluidic Preparation of DiI-Loaded PCL-*b*-PEO Nanoparticles. For microfluidic preparation of nanoparticles loaded with dye, three different streams were combined with an Ar gas stream to form gas-segmented liquid plugs. The following three fluid streams were combined ~~at equal flow rate~~ to form gas-segmented liquid plugs within the reactor: (1) either a 1.0 wt % solution of PCL-*b*-PEO in DMF (for cwc + 10 wt % case) or a 3.3 wt % solution of PCL-*b*-PEO in DMF (for cwc + 75 wt % case) with DiI codissolved at a dye:copolymer ratio of 0.02 in both cases; (2) a separator stream containing DMF only; and (3) a water-containing stream consisting of either a DMF solution containing 46.5 wt % deionized water (for cwc + 10 wt % case) or pure deionized water (for cwc + 75 wt % case). Combination of the three liquid streams at equal flow rate yielded ~~a steady-state on-chip copolymer concentration of 0.33 wt % and~~ a steady-state water concentration of ~~either~~ 15.5 wt %; combination of the three liquid streams at a flow rate ratio of 10:10:80 yielded a steady-state water concentration of~~or~~ 80.5 wt %. These two on-chip water concentrations corresponded to cwc + 10 wt % and cwc + 75 wt %, respectively, where the measured cwc of the copolymer solution was determined to be 5.5 wt %. For both water concentrations, the steady-state on-chip copolymer concentration was 0.33 wt %. Microfluidic flow conditions were selected and controlled as described in the previous section.

Nanoparticle samples with loaded dye were collected from the reactor into vials containing a 10×-excess volume of deionized water, followed by 12 h dialysis (overnight dialysis) against deionized water (with changing of water every hour for the first 4 h of dialysis) to remove residual DMF and unencapsulated DiI. The extremely small amounts of DMF remaining in the nanoparticles following dialysis is not expected to contribute to cell toxicity in a drug delivery application. However, this question is currently being investigated by *in vitro* cytotoxicity studies in our lab, which will be reported in a forthcoming publication. The resulting aqueous dispersions of DiI-loaded nanoparticles were analyzed by TEM, XRD, and DLS, and

loading efficiencies and release kinetics were determined using fluorescence spectroscopy.

Transmission Electron Microscopy. Transmission electron microscopy (TEM) was performed using a JEOL JEM-1400 TEM, operating at an accelerating voltage of 65 kV and equipped with a Gatan Orius SC1000 CCD camera. TEM images were obtained by depositing diluted dispersions (~0.03 wt % copolymer) consisting of DiI-loaded PCL-*b*-PEO nanoparticles in water onto carbon-coated 300 mesh copper TEM grids as described below.

To improve contrast, uranyl acetate was used to negatively stain the PCL-*b*-PEO nanoparticles. Uranyl acetate selectively binds to the PEO coronal chains, providing reverse contrast for the PCL cores, which appear white in TEM images of stained samples. For reverse staining experiments, nanoparticle dispersions were mixed with 1 wt % aqueous solution of uranyl acetate in a 1:1 ratio (v/v) and one drop of the resulting mixture was deposited onto a TEM grid. Excess liquid was immediately removed using lens paper, followed by drying of remaining liquid under ambient conditions.

Due to the high electron density of uranyl acetate, negative staining generally impedes visualization of internal lumen of vesicle structures, such that vesicles and spheres cannot be readily distinguished from stained samples. Therefore, all samples revealing aggregates of spherical shape in negative contrast TEM images were also imaged without staining. In unstained images, contrast is provided by high density PCL crystallites which appear dark relative to both the background and the internal lumen of vesicles, such that vesicles appear hollow in unstained images and so can be differentiated from spheres. We find that one complication of imaging PCL-*b*-PEO nanoparticles without staining is that upon drying under ambient conditions, deposited dispersions form large crystallites of PEO which obscure identification of micellar PCL cores. To avoid this problem, micellar dispersions deposited without reverse staining were freeze-dried on TEM grids using the following method. First, one drop of the micellar dispersion was deposited onto a TEM grid and excess liquid was immediately removed using lens paper. The remaining liquid was then vitrified by submerging the TEM grid into liquid ethane. The resulting vitrified sample was then freeze-dried under vacuum. As discussed below, the morphological identification of some aggregates required the evaluation of their heights. For these experiments, Pt/Pd shadowing of unstained aggregates following freeze-drying on the grid was carried out at a shadowing angle of 45°.

For each set of conditions (water content and flow rate), reported prominent morphologies and mean dimensions from TEM of nanoparticles with loaded DiI (Table 1) were determined from TEM analysis of three separate preparations starting with three individually-prepared stock solutions. For each sample preparation and TEM grid deposition method (unstained, stained, and shadowed), at least 2-3 TEM images taken in different regions of the grid were evaluated. Prominent morphologies for each condition were assigned based on the following definitions with associated evaluation methods in brackets. Spheres were defined as aggregates with circular projections (TEM with staining) but without internal lumen (TEM without staining). Vesicles were defined as aggregates with circular projections (TEM with staining) with internal lumen (TEM without staining). Cylinders were defined as high aspect-ratio filaments of approximately regular width (TEM with staining). Lamellae were defined as irregularly-shaped aggregates (TEM with staining) with heights significantly smaller than their lateral dimensions (TEM with shadowing); from cases where aggregate shadowing was carried out, lamellae heights were determined to be 9 nm (Figure S2). For each preparation, mean dimensions were determined from ~400 particles; therefore, for each of the mean dimensions in Table 1, N = 400 × 3 preparations = ~1200, such that the reported errors reflect reproducibility of the preparation method. Mean sphere diameters and cylinder widths were determined exclusively from TEM images with staining. Averaging and statistical analysis of dimensions from TEM images was conducted using Image J software.

Dynamic Light Scattering. Effective hydrodynamic diameters of DiI-loaded PCL-*b*-PEO nanoparticles were determined using dynamic light scattering (DLS). DLS measurements were carried out using a Brookhaven Instruments photon correlation spectrometer equipped with a BI-200SM goniometer, a BI-9000AT digital autocorrelator, and a Melles Griot He-Ne Laser (633 nm) with a maximum power output of 75 mW. All DLS measurements of DiI-loaded nanoparticles were performed in pure water and an experimental temperature of 23°C and at a scattering angle of 90°.

After overnight dialysis against deionized water to remove residual DMF and unencapsulated DiI, the DiI-loaded nanoparticles were transferred to pre-cleaned scintillation vials then diluted 5× using deionized water, filtered through two nylon syringe filters in series with nominal pore sizes of 0.2 m (National Scientific Company) to give a final copolymer concentration of ~0.07 mg/mL. For each nanoparticle preparation, mean effective hydrodynamic sizes were determined from three measurements of the autocorrelation function using cumulent analysis. Mean effective hydrodynamic diameters were determined from three separate data collections corresponding to one individually-prepared stock solution, such that reported errors reflect the error in data collection.

X-Ray Diffraction. X-ray diffraction measurements were performed on a Rigaku Miniflex diffractometer with a Cr source (kR radiation, λ = 2.2890 Å) operating at 30 kV and 15 mA with a resolution of 0.05° (2θ) and a scan speed of 1°/min. X-ray diffraction profiles were collected for 2θ ranging from 10-80 degrees.

For XRD sample preparation, water was removed from suspensions of DiI-loaded nanoparticles by rotory evapo-

ration at 25 °C until solid films were obtained. The resulting films were then scraped as a powder into the XRD specimen holder with no subsequent drying step to remove residual solvent. We note that this preparation method will significantly increase the crystallinity of coronal PEO blocks relative to their colloidal state, as removal of water from the nanoparticle coronae will allow initially-solubilized PEO chains to pack together. However, since the hydrophobic cores will contain no water in the purely aqueous suspensions, we do not expect the crystallinity of the core-forming PCL blocks to be strongly affected when water is removed by rotory evaporation. Therefore, our XRD experiments should provide a reasonable probe of nanoparticle core crystallinity in the colloidal state.

Peak deconvolution of XRD data was done using Origin Pro Version 8.1. Two characteristic reflections for each of crystalline PCL and crystalline PEO were identified from the literature and these were used to fix the positions of four Lorentzian peak contributions to the fit;[58,20] another small Lorentzian peak contribution was used to account for a small shoulder on the more intense PCL peak in order to obtain a good fit (Figure S3). Thus, XRD data were fit to a sum of 6 Lorentzian functions: 3 peaks assigned to crystalline PCL (2θ = 32.5, 32.7, and 35.7), 2 peaks assigned to crystalline PEO (2θ = 29.2 , 35.4), and 1 peak (no fixed position) assigned to incoherent scattering from amorphous copolymer (amorphous halo). Areal peak contributions from the three components (crystalline PCL, crystalline PEO, and amorphous copolymer) were then determined by integration and percentages of crystalline PCL and PEO were calculated using:

$$\%\ \textit{Crystalline}\ \text{PCL} = A_{\text{PCL}}/A_{\text{total}},\ \text{and}\ \%\ \textit{Crystalline}\ \text{PEO} = A_{\text{PEO}}/A_{\text{total}},$$

where $A_{\text{total}} = A_{\text{PCL}} + A_{\text{PEO}} + A_{\text{amorph.}}$

DiI Loading Efficiency Determination. To determine the dye loading efficiency, DiI-loaded nanoparticles were dissolved by adding a small weighed aliquot of the nanoparticle dispersion (1 – 2 drops) to a known quantity of DMF (selected so that maximum absorbance values were ≤ 0.1) and stirring for 4 h in the dark. Fluorescence intensity – concentration calibration curves for DiI at the emission maximum (λ_{ex} = 549 nm; λ_{em} = 565 nm, Figure S4) in DMF solutions were determined in the linear range; fluorescence intensities of dissolved nanoparticle solutions were measured at the same wavelengths and under identical conditions to those of the calibration standards, and within 5 min of obtaining the calibration curves. Before calculating integrated photoluminescence intensities, a solvent background was subtracted and a correction for the detector response was applied to each sample and standard measurement. The dye concentrations were then determined from the calibration curves. After correcting for dilution factors, the loading efficiency was determined using the following expression:

$$\text{loading efficiency (\%)} = \frac{\text{DiI in micelles (g)}}{\text{total DiI used (g)}} \times 100\%$$

Errors on loading efficiencies were calculated from standard deviations of values for three repeat preparations of DiI-loaded nanoparticles under the same chemical and flow conditions.

Determination of DiI Release Kinetics Under Perfect Sink Conditions. Dye release kinetics for nanoparticles prepared at various flow rates and two different water contents were determined under perfect sink conditions. For these experiments, a dialysis bag (MWCO: 50 kDa, Spectrum Labs) containing a 1.5 g suspension of DiI-loaded nanoparticles was placed in a 250 mL beaker filled with tap water. The beaker was then placed in a crystallization dish (190 x 100) equipped with a valve for outflowing water. Tap water (4 ˚C, pH = 5.4) was allowed to flow into the beaker at ~480 mL/min via a Tygon tube. The beaker was allowed to overflow into the crystallization dish and subsequently flow out into the sink. At various times, *t*, aliquots of the dye-loaded nanoparticles were taken out of the dialysis bag. The sample was then put into a quartz microcuvette and subsequently analyzed using fluorescence spectroscopy (λ_{ex} = 549 nm; λ_{em} = 565 nm) to determine I(t). After analysis, the aliquot of dye-loaded nanoparticles was returned to the dialysis bag and perfect sink conditions.

Release Experiments into Various Media. In order to determine the effect of the release medium on the release kinetics of the dye, release experiments for a single sample of DiI-loaded nanoparticles prepared at a water content of cwc + 10 wt % and a flow rate of 100 µL/min were carried out into the following media at the indicated temperatures: 1. perfect sink conditions, 4 ˚C, pH = 5.4; 2. deionized water, 23 ˚C, pH = 6.7; 3. 1% PBS, 23 ˚C, pH = 7.4; 4. 1% PBS + albumin (Sigma Aldrich) (45 g / L), 23 ˚C, pH = 7.4; 5. 1% PBS + albumin (Sigma Aldrich) (45 g / L), 37 ˚C, pH = 7.4; 6. 1% PBS + albumin (Sigma Aldrich) (45 g / L), 37 ˚C, pH = 4.0; and 7. 1% PBS + cell lysate (protein concentration = 0.38 g / L), 37 ˚C, pH = 7.4. The pH of all PBS-containing solutions was adjusted to either 7.4 or 4.0 using either HCl or NaOH before the release was started.

For all release experiments except those under perfect sink conditions, which are described in the previous section, the following procedures were applied. DiI-loaded nanoparticle dispersions (~10 mL) were transferred to a dialysis bag (SpectrumLabs, MWCO 100 kDa) which was placed into a reservoir containing 250× volume excess of a particular release medium compared to the DiI-loaded nanoparticle dispersions. Throughout the release experiments, the release medium was constantly stirred using magnetic stirring and maintained at experimental temperature using a hot plate in conjunction with a thermocouple. At predetermined times, aliquots of the sample were removed from the dialysis bag, air dried, and dissolved into DMF followed by DiI quantification using fluorescence spectroscopy (λ_{ex} = 549 nm; λ_{em} = 565 nm). For aliquots containing albumin or PBS, a liquid- liquid extraction using methyl *tert*-butyl ether (Sigma Aldrich) was conducted to extract DiI from the media solution. Prior to quantifying the amount of DiI obtained from liq-

uid-liquid extraction, triplicate control experiments were conducted to determine the efficiency of the liquid-liquid extraction: known amounts of DiI were mixed in with a solution containing both albumin and PBS, then a liquid-liquid extraction was conducted using methyl tert-butyl ether: the amount of DiI recovered was calculated to be >95% (w/w).

To prepare the cell lysate, the MCF-7 human adenocarcinoma breast cancer cell line was obtained as a generous gift from the BC Cancer agency. Cells were grown in Dulbecco's Modified Eagle's Medium (DMEM) supplemented with 10% fetal bovine serum in a 175 cm^2 culture flask and maintained at 37 °C with 5% CO_2 in a tissue culture incubator. To lyse the cells, the cells were exposed to lysis buffer (0.5% Triton X- 100, 0.5% NP-40, 0.15 M NaCl, 0.05 M Tris pH 8, and 0.001 M EDTA) and supplemented with a protease inhibitor cocktail set III (Millipore). The lysate protein concentration was quantified using the Bradford assay (Bio-Rad),[59,60] using bovine serum albumin (BSA) as a standard. In brief, the cell lysate (5 µL) was combined with the Bradford assay reagent (1 mL) and then analyzed for the protein concentration by monitoring absorbance at 595 nm.

RESULTS AND DISCUSSION

Effect of Flow Rate on Multiscale Structure of DiI-Loaded Nanoparticles. Figure 2 presents the influence of on-chip flow rate on nanoparticle morphologies from TEM images and corresponding hydrodynamic size distributions from CONTIN analysis of DLS data. For two different water contents, both nanoparticle morphologies and hydrodynamic sizes show very similar trends with increasing flow rate. Starting with nanoparticles prepared at an on-chip flow rate of 25 µL/min, TEM shows a combination of small spheres, lamellae and long filaments (Figure 2, A and D); the corresponding DLS size distributions show three distinct populations at ~70 nm, ~800 nm, and ~2000 nm, which we attribute to spheres, lamellae, and filaments, respectively, based on their lateral dimensions from TEM. When the flow rate is increased to 50 µL/min, we find that long filaments are no longer present in the TEM images (Figure 2, B and E) but that spheres and lamellae persist; this is also supported by the DLS results, which show only two particle populations at ~70 nm and ~1000 nm. Finally, at a flow rate of 100 µL/min (Figure 2, C and F), the long filaments return and all three morphologies (spheres, lamellae and filaments) are again present in the TEM images with three distinct populations observed by DLS. Table 1 lists morphologies and mean dimensions for each set of conditions, with excellent reproducibility observed over multiple preparations (Figures S5 and S6).

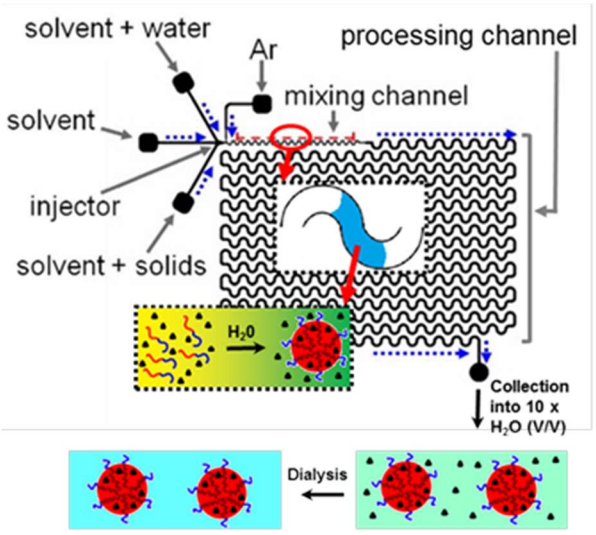

Figure 1. Schematic of the gas-liquid segmented reactor and on-chip formation of DiI-loaded PCL-*b*-PEO nanoparticles.

Table 1. Morphologies[a] and Mean Dimensions[b] for PCL-*b*-PEO Nanoparticles Prepared in the Segmented Microfluidic Reactor at Various Water Contents and Flow Rates.

Water Content (cwc + *x* wt %)	25 µL/min	50 µL/min	100 µL/min
10	S (48 ± 4 nm) + C (15 ± 3 nm) + L	S (51 ± 5 nm) + L	S (47 ± 4 nm)+ C (16 ± 4 nm) + L
75	S (46 ± 5 nm) + C (15 ± 3 nm) + L	S (49 ± 4 nm) + L	S (49 ± 4 nm)+ C (14 ± 3 nm) + L

a) Prominent morphologies are indicated as S (spheres), C (cylinders or filomicelles), and L (lamellae).

b) Numbers refer to mean sphere diameters and cylinder widths. Reported errors are standard deviations of mean values determined for three replicate preparations.

The nonmonotonic trend in nanoparticle morphologies on the colloidal length scale, with long filaments first disappearing and then reappearing with increasing on-chip flow rate, is in contrast to the corresponding linear behaviour of the internal crystallinity of nanoparticles at the nanoscale. Figure 3 shows a clear linear increase in PCL crystallinity versus flow rate for both water contents. These data include the three flow rates discussed in Fig-

ure 2 along with additional flow rates to confirm the linear trend.

Effect of Water Content on Multiscale Structure of DiI-Loaded Nanoparticles. Considering the effect of on-chip water content during nanoparticle formation, Figure 2 shows very similar nanoparticle morphologies and sizes for two vastly different water contents, cwc + 10 wt % and cwc + 75 wt %, at each of the three on-chip flow rates. This indicates a minimal influence of water content on the size and structure of DiI-loaded nanoparticles on the colloidal length scale. However, at the nanoscale, Figure 3 show that mass of crystalline PCL within the micelles is 15-30 % higher at lower water content compared to higher water content over the range of investigated flow rates.

Discussion of Effects of Flow Rate and Water Content on Multiscale Structure of DiI-Loaded Nanoparticles. The effects of on-chip flow rate on the size, morphology and internal crystallinity of block copolymer nanoparticles formed in segmented gas-liquid microfluidic reactors have been described in our previous publica-

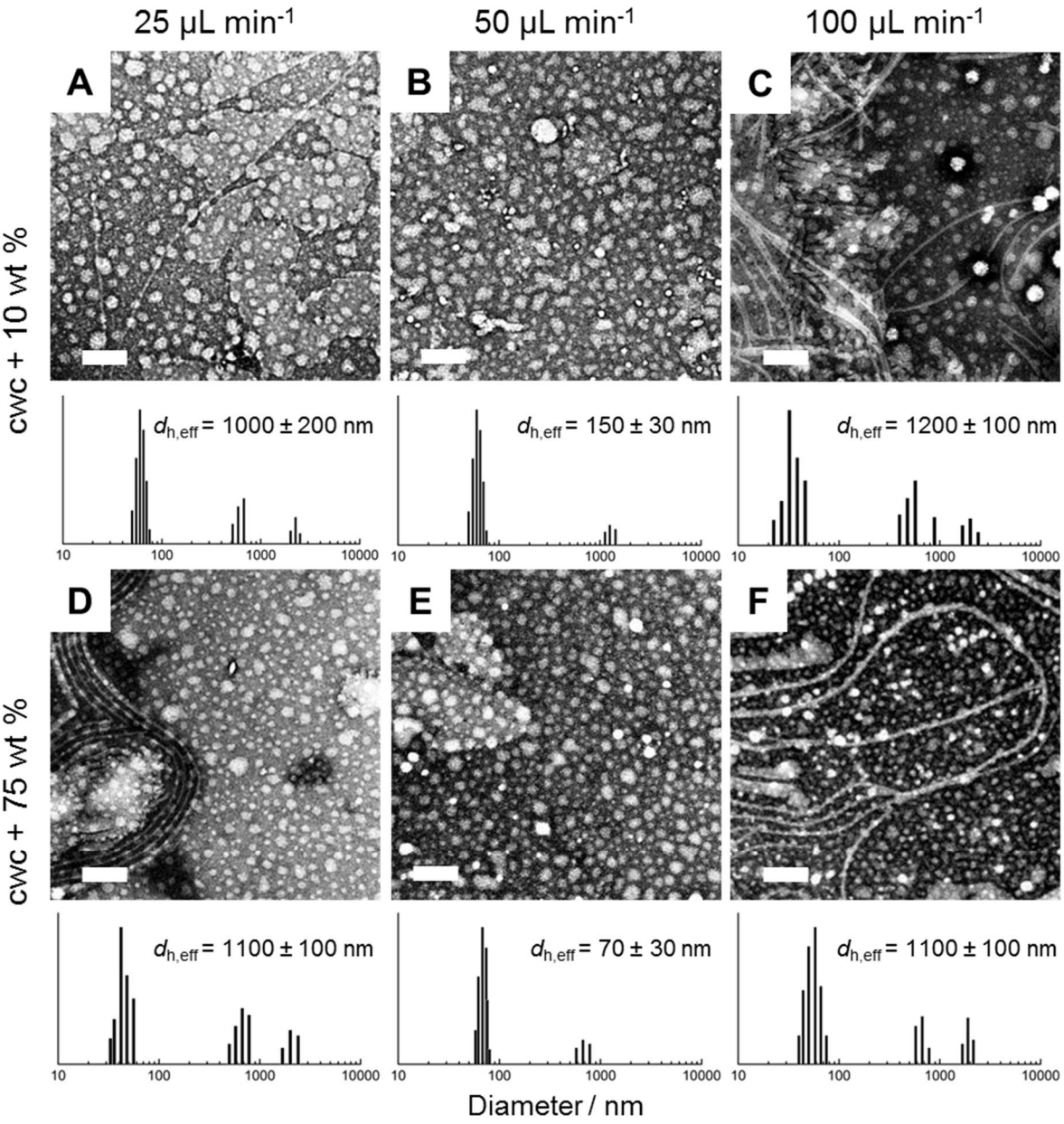

Figure 2. Effect of flow rate and water content on morphology and hydrodynamic size of DiI-loaded PCL-*b*-PEO nanoparticles. TEM images were produced by negative staining with uranyl acetate. All scale bars are 200 nm. Below each TEM image is a representative size distribution obtained from CONTIN analysis of DLS autocorrelation functions, along with the mean effective hydrodynamic diameter determined from CUMULENT analysis.

tions.[27,30,20] Flow effects are attributed to the influence of high-shear "hot spots" on the evolution of polymeric nanoparticles as they progress through the processing channel (Figure 1) following their initial formation due to water mixing in the mixing channel. Three main mechanisms have been described by which hot spots can affect the final size and structure of polymeric nanoparticles: 1. shear-induced breakup of larger particles followed by intraparticle chain rearrangements; 2. shear-induced coalescence of smaller particles followed by intraparticle chain rearrangements; and 3. shear-induced crystallization. The first mechanism favours lower aggregation numbers with increasing flow rate, whereas the last two mechanisms favour higher aggregation numbers with increasing flow rate. The relative importance of these three mechanisms depends on a number of factors, including the maximum shear rate and the sizes, morphologies, and internal viscosities of the initially-formed nanoparticles.[20,27,30]

Our previous work on PCL-*b*-PEO nanoparticles without hydrophobic molecules loaded in the cores showed nonmonotonic trends in morphology and size with respect to on-chip flow rate which were attributed to the competition between these flow-directed mechanisms.[20] In the present case, the disappearance of long filaments between 25 µL/min (Figure 2, A and D) and 50 µL/min (Figure 2, B and E), and the corresponding decrease in hydrodynamic size, is explained by the increased importance of shear-induced breakup of filaments in this range of flow rates. Then, when the flow rate is increased to 100 µL/min (Figure 2, C and F), the reappearance of filaments and increase in hydrodynamic size can be explained by an increased rate of either shear-induced coalescence or shear-induced crystallization or a combination of both mechanisms. In contrast, our work on microfluidic-prepared PAX-loaded PCL-*b*-PEO nanoparticles showed a monotonic trend of increasing nanoparticle hydrodynamic size with increasing flow rate, although the both the water content (cwc + 5 wt %) and loading ratio (drug:polymer = 0.01) during nanoparticle formation were both lower than in the present case.[20] However, this difference does highlight potential differences between results obtained using dye surrogates and those obtained for specific drug targets; it also emphasizes that although dyes such as DiI may be useful for preliminary screening of on-chip manufacturing conditions, they will not eliminate the need for optimization experiments employing the specific molecule of interest.

We have previously reported a linear increase in the crystallinity of PCL cores with on-chip flow rate for both nanoparticles formed without hydrophobic cargo and with PAX loaded in the cores.[20] This was explained by shear-induced crystallization in the processing channel as micelles formed in the mixing channel are exposed to the high-shear hot spots, where transient and elastic nanoparticle deformations may increase the orientation and crystallization of PCL chains. Here we find that a similar linear trend exists for DiI-loaded nanoparticles formed at both low (cwc + 10 wt %) and high (cwc + 75 wt %) water contents (Figure 3). Moreover, the overall higher PCL crystallinities for nanoparticles formed at the higher water content can be explained by the lower DMF solvent in the PCL phase under these conditions, allowing the less plasticized PCL to crystallize more readily. These results indicate that for the microfluidic formation of PCL-*b*-PEO nanoparticles containing various hydrophobic cargo molecules, both the water content and flow rate will be critical manufacturing parameters.

Effect of Flow Rate and Water Content on DiI Loading Efficiency. Loading efficiencies of DiI within nanoparticles prepared at three different flow rates (25, 50, and 100 µL/min) and two different water contents (cwc + 10 wt % and cwc + 75 wt %) are shown in Figure 4. Loading efficiency data obtained for nanoparticles prepared at additional flow rates between 5 and 120 µL/min are shown in Figure S7. At the lower water content (cwc + 10 wt %),

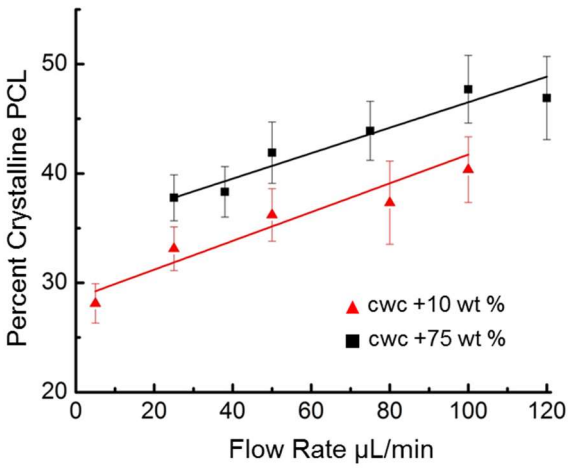

Figure 3. Effect of flow rate and water content on PCL crystallinity within the cores of DiI-loaded PCL-*b*-PEO nanoparticles

loading efficiencies increase monotonically with increasing on-chip flow rate, starting at 76 % at 25 µL/min, then jumping to 90 % at 50 µL/min, then further increasing slightly to 94 % at 100 µL/min. Interestingly, we previously reported a similar trend of increasing loading efficiency with increasing on-chip flow rate for the drug PAX at a similarly-low water content (cwc + 5 wt %), despite differences in flow dependencies of size and morphology for PAX- and DiI-loaded nanoparticles.[20] At the high water content (cwc + 75 wt %), loading efficiencies are significantly lower than at the low water content, and also show a nonmonotomic trend with increasing flow rate, starting at 52 % at 25 µL/min, then dropping to 43% at 50 µL/min, then jumping back to 53 % at 100 µL/min.

Based on thermodynamics alone, the higher water content should lead to a higher interfacial tension between the PCL core and the surrounding aqueous environment, and therefore a stronger partitioning of hydrophobic DiI into the core. However, we find instead that the lower

water content leads to consistently higher loading efficiencies (Figure 4). This can be partially explained by the role of kinetics in the partitioning of the dye into the nanoparticle cores: at lower water content, the cores are more highly swollen with DMF, which lowers their viscosities and facilitates the diffusion of dye into the cores. Also, the ordered PCL chains within crystallites will exclude guest dye molecules; therefore the higher PCL crystallinities at higher water content (Figure 3) could contribute to the lower DiI solubilities within the cores.

The effect of on-chip flow rate on loading efficiency is found to be different at the lower and higher water contents. At the higher water content (cwc + 75 wt %), the loading efficiency tracks with the mean size of nanoparticles (Figure 2, D-F), first decreasing and then increasing with increasing flow rate (Figure 4). Larger hydrophobic cores are known to show higher solubility for hydrophobic molecules,[25,61] which can explain this tracking of loading efficiency with nanoparticle size. In contrast, at the lower water content (cwc + 10 wt %), where the loading efficiencies are generally much higher, loading efficiencies are found to increase steadily with flow rate rate, despite a similar nonmonotonic trend in nanoparticle size as the the cwc + 75 wt % case (Figure 2, A-C). This suggests that DiI solubility is not strongly tied to nanoparticle size at the lower water content, probably due to the strong swelling of PCL cores with DMF in this case. Our understanding of the increase in loading efficiency with flow rate in the cwc + 10 wt % case (Figure 4) is unclear, although this trend may be due in part to a positive effect of increased mixing rate under higher shear conditions on dye loading.

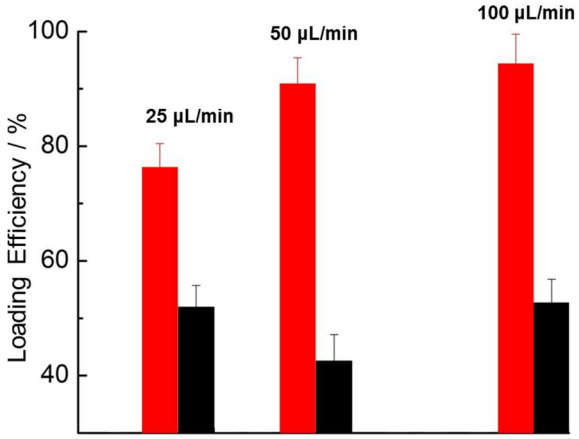

Figure 4. Effect of flow rate and water content on the loading efficiency of DiI-loaded PCL-*b*-PEO nanoparticles. Red bars: nanoparticles prepared at cwc + 10 wt %; black bars: nanoparticles prepared at cwc + 75 wt %.

Effect of Flow Rate and Water Content on DiI Release Kinetics. Similar to loading efficiencies, DiI release kinetics under perfect sink conditions show different on-chip flow rate dependencies at the high and low water contents. DiI release profiles at three different flow rates and at two different water contents are shown in Figure 5. Nanoparticles formed at the lower water content (cwc + 10 wt %) show generally faster release kinetics, with complete DiI release occurring in the range of ~2-4 days (Figure 5A). This is in contrast to nanoparticles formed at the higher water content (cwc + 75 wt %), which required a minimum of 15 days for dye release and some cases showing incomplete release even after 20 days (Figure 5B).

For the cwc + 10 wt % nanoparticles (Figure 5A), dye release becomes progressively slower with increasing flow rate of on-chip manufacturing. Nanoparticles formed at the lowest flow rate (25 µL/min) show the fastest dye release, with $t_{1/2}$ = 30 min and 100 % release after ~2 days. For the intermediate flow rate of 50 µL/min, the release is significantly slower, with $t_{1/2}$ = 3 h and ~3.5 days required for complete release. Finally, at the highest flow rate of 100 µL/min, dye release is slower still, with with $t_{1/2}$ = 4 h and 100 % release achieved after ~4 days.

On the other hand, nanoparticles formed at cwc + 75 wt % (Figure 5B) show release kinetics that first decrease and then increase with increasing flow rate. Nanoparticles formed at 25 µL/min show release of DiI with $t_{1/2}$ = 5 h and a maximum of ~95 % dye released after 22 days. When the flow rate is increased to 50 µL/min, a decrease in dye release rate is observed, with $t_{1/2}$ = 7 h and a maximum of ~85 % dye released after 22 days. However, when the flow rate is further increased to 100 µL/min, the resulting nanoparticles show a sharp increase in release kinetics and the fastest dye release at this water content, with with $t_{1/2}$ = 2 hrs and 100 % release achieved after ~17 days (Figure 5B).

Discussion of the Relationship Between Multiscale Structure and DiI Release Kinetics. The described trends in release kinetics with respect to both the flow rate and water content of nanoparticle formation should be directly tied to the multiscale structure of the nanoparticles. Based on previous observations from our group and elsewhere in the literature,[12,13,55,18,19,61,20] three specific aspects of nanoparticle structure will influence the release kinetics of hydrophobic molecules from the core: 1. core volume; 2. core morphology; and 3. internal core crystallinity. For diffusional release, both core volume and morphology (through the surface-to-volume ratio) will influence diffusional distances of molecules to escape the hydrophobic cores. Core crystallinity has been shown to have a direct correlation with internal core viscosity, which will influence diffusion coefficients within the cores. In addition, all three structural factors (volume, morphology and crystallinity) will affect the kinetics of hydrolytic nanoparticle degradation which, along with simple diffusion, provides another mechanism of release.[16,20]

First considering the effect of water content on release kinetics, the significantly faster release at the lower water content (cwc + 10 wt %, Figure 5A) compared to the higher water content (cwc + 75 wt %, Figure 5B) is explained by the corresponding lower PCL crystallinities in the former case (Figure 3). Higher PCL crystallinity has been previously shown to increase the microviscosity of the nanoparticle core, leading to slower diffusion of encapsulated molecules and correspondingly slower release kinetics.[12,13,19,20] In addition to slower release, the high PCL crystallinity appears to result in the kinetic trapping of DiI molecules within the cores of two of the three cwc + 75 wt % samples, as evinced by the leveling off of release levels at ~95 % and ~85 % after ~20 days for the 25 µL/min and 50 µL/min nanoparticles, respectively (Figure 5B).

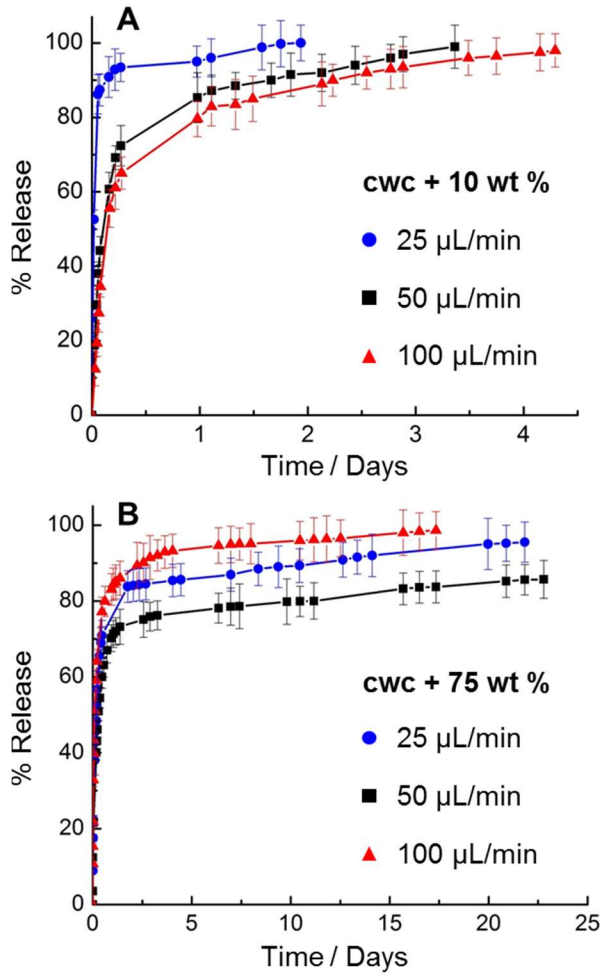

Figure 5. Effect of flow rate and water content on the release of DiI from DiI-loaded PCL-*b*-PEO nanoparticles. (A) Release profiles for nanoparticles prepared at cwc + 10 wt % and various flow rates. (B) Release profiles for nanoparticles prepared at cwc + 75 wt % and various flow rates. All release experiments carried out under perfect sink conditions as described in the text.

We next consider the effect of on-chip flow rate on release kinetics at a water content of cwc + 10 wt % (Figure 5A). The observed monotonic slowing down of release kinetics with increasing flow rate can be explained by the concomitant increase in core crystallinity (Figure 3), which will lead to a corresponding increase in core viscosity and decrease in the diffusion coefficient of DiI within the cores. Since neither nanoparticle size nor morphology track with the DiI release rates at this water content, it appears that, of the three structural parameters listed above, the role of core crystallinity is most important in determining the flow dependence of release kinetics under these conditions. We find that this monotonic trend of slower release kinetics with increasing on-chip flow rate agrees with results obtained previously for PAX-loaded nanoparticles prepared in an identical microfluidic reactor at a low but slightly different water content (cwc + 5 wt %).[20]

Finally, we consider the nonmonotonic effect of on-chip flow rate on the release kinetics of nanoparticles prepared at a water content of cwc + 75 wt % (Figure 5B). Interestingly, the slowest release kinetics at this water content are shown by nanoparticles prepared at the intermediate flow rate (50 µL/min), which is the one flow rate that does not produce a significant number of filaments, as discussed previously (Figure 2E). In previous work, the hydrolytic degradation of filaments has been shown to occur more rapidly than other morphologies, providing an additional pathway for faster release of DiI.[20] The tracking of the availability of this pathway with the presence of filament nanoparticles thus explains the observed flow dependence of release kinetics.

Effect of Release Media on DiI Release Kinetics. Along with release kinetics under perfect sink conditions described above (flowing tap water, 4 °C, pH = 5.4), for a single DiI-loaded nanoparticle sample we also investigated release into a variety of media at different temperatures meant to mimic physiological conditions to various extents. For all release media except perfect sink conditions, the aqueous reservoir was static (i.e. not continually replenished) although a strong concentration gradient was maintained through a large volume differential (250×) in favour of the release medium compared to the dialyzing sample.

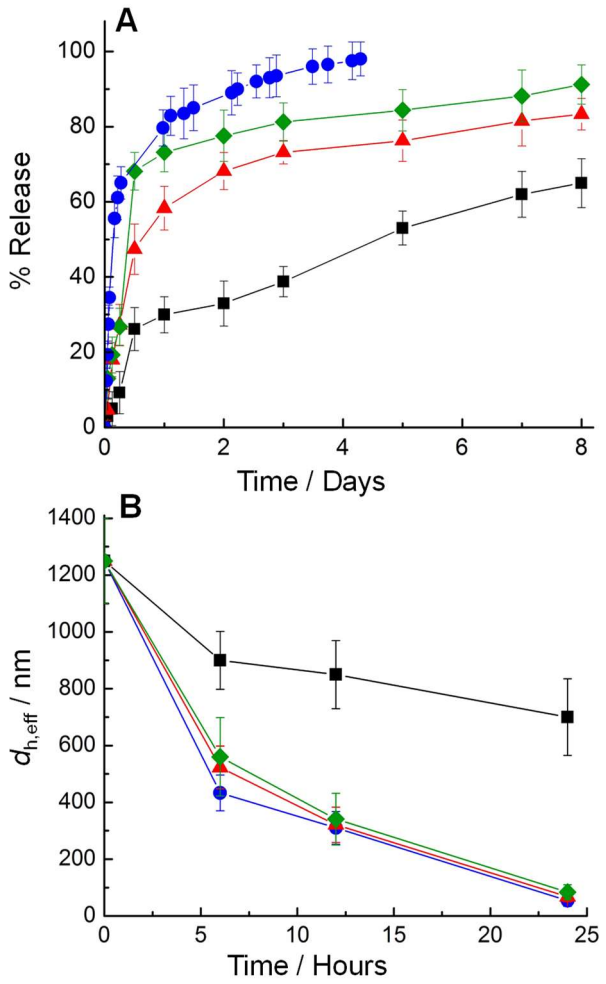

Figure 6. Effect of different chemical and physical characteristics of release media on DiI release profiles (A) and decay of nanoparticle hydrodynamic size (B) for DiI-loaded PCL-*b*-PEO nanoparticles assembled on-chip at a flow rate of 100 µL/min and a water content of cwc + 10 wt %. In both (A) and (B), the release media are as follows: 1. perfect sink conditions, 4 °C, pH = 5.4 (●); 2. deionized water, 23 °C, pH = 6.7 (■); 3. PBS buffer, 23 °C, pH = 7.4 (▲); and 4. PBS buffer + albumin, 23 °C, pH = 7.4 (◆).

First, release kinetics under perfect sink conditions were compared with release into various aqueous reservoirs at room temperature (deionized water, pH = 6.7; PBS buffer only, pH = 7.4; and PBS buffer + albumin, pH = 7.4). The resulting four release profiles are shown in Figure 6A. Due to the importance of hydrolytic nanoparticle degradation to release kinetics, the hydrodynamic nanoparticle sizes under the various conditions were also tracked by DLS for the first 24 h of release and the corresponding plots are shown in Figure 6B. Of the four release profiles (Figure 6A), perfect sink conditions at pH = 5.4 show fastest release (blue curve, $t_{1/2}$ = 4 h), followed by PBS buffer + albumin at pH = 7.4 (green curve, $t_{1/2}$ = 10 h), then PBS only at pH = 7.4 (red curve, $t_{1/2}$ = 13 h), and finally deionized water at pH = 6.7, which shows significantly slower release than the other four conditions (black curve, $t_{1/2}$ = 5 days). From the corresponding plots of nanoparticle size (Figure 6B), we find that deionized water also leads to the slowest rate of size decrease, suggesting slowest hydrolytic degradation of the nanoparticles, with the other three conditions showing similar rates of nanoparticle degradation within experimental error.

From these results, we conclude that the main bottleneck for the significantly slower release into deionized water is the correspondingly slow rate of nanoparticle degradation under these conditions. This underlines the importance of hydrolytic degradation to the release of hydrophobic molecules from PCL-*b*-PEO nanoparticles. It also suggests that the presence of ions in the aqueous media, such as are present in tap water and all solutions containing PBS but not in deionized water, play an important catalytic role in the hydrolysis reaction. The significant but more subtle differences in the other three conditions, which show essentially identical degradation rates in the first 24 h, indicate that other aspects of the release media also play a role in influencing the release. For example, the fastest release rate occurring for perfect sink conditions is attributed to the continual replenishing of the release media and the maintenance of an infinite chemical potential gradient in that experiment. The slightly higher release rate into PBS + albumin compared to PBS alone is ascribed to the hydrophobic surface of the albumin protein allowing adhesion of the hydrophobic dye and facilitating transport through the aqueous medium.

Next, release kinetics were compared for various aqueous reservoirs at physiological temperature (37°C, PBS + albumin, pH = 4.0; PBS + albumin, pH = 7.4; and PBS + cell lysate, pH = 7.4), along with room temperature release into PBS + albumin at pH = 7.4. The resulting four release profiles are shown in Figure 7A with corresponding plots of nanoparticle size in Figure 7B. Of the three release profiles obtained at 37°C (Figure 7A, solid curves), PBS + albumin at pH = 4.0 showed the fastest release (purple curve, $t_{1/2}$ = 8 h), followed by PBS + albumin at pH = 7.4 (orange curve, $t_{1/2}$ = 9 h), then PBS + cell lysate at pH = 7.4 (gray curve, $t_{1/2}$ = 12 h). Comparing identical chemical conditions at two different temperatures, DiI release into PBS + albumin at pH = 7.4 and room temperature (dashed green curve, $t_{1/2}$ = 10 h) is slightly slower than release into the same medium at physiological temperature (orange curve, $t_{1/2}$ = 9 h); this can be attributed to a marginally faster rate of hydrolytic degradation at the more elevated temperature, as indicated by the corresponding plots of nanoparticle size in Figure 7B.

We note that the effect of acidic pH into otherwise equivalent solutions of PBS + albumin is a slight increase in release rate (Figure 7A, purple and orange curves, pH = 4.0 and 7.4, respectively) which can be attributed to an increased rate of PCL hydrolysis under acidic conditions. However, if the rate of hydrolysis is faster at pH = 4.0 than at 7.4 under these conditions, this is not reflected in the corresponding plots in Figure 7B, which show similar rates of decreasing nanoparticle size in these two cases;

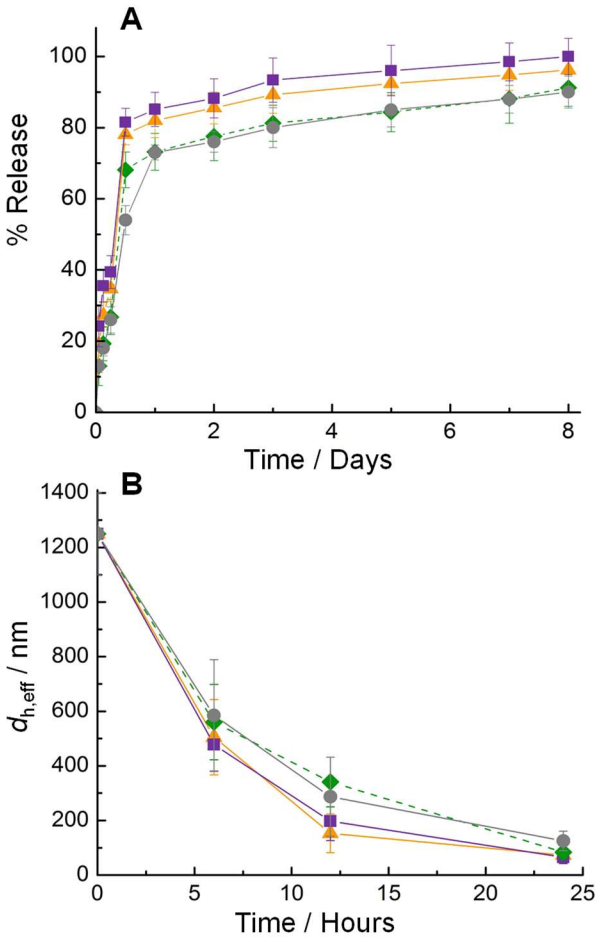

Figure 7. Effect of different chemical and physical characteristics of release media on DiI release profiles (A) and decay of nanoparticle hydrodynamic size (B) for DiI-loaded PCL-*b*-PEO nanoparticles assembled on-chip at a flow rate of 100 µL/min and a water content of cwc + 10 wt %. In both (A) and (B), the release media are as follows: 1. PBS buffer + albumin, 23 ˚C, pH = 7.4 (◆); 2. PBS buffer + albumin, 37 ˚C, pH = 7.4 (▲); 3. PBS buffer + albumin, 37 ˚C, pH = 4.0 (■); 4. PBS buffer + cell lysate, 37 ˚C, pH = 7.4 (●).

one possibility is that pathways of PLC hydrolytic degradation that contribute to DiI release but do not significantly affect hydrodynamic diameter, such as poration, are selectively accelerated at decreased pH. Finally, the relatively slow rate of release into PBS + cell lysate at pH = 7.4 compared to PBS + albumin at pH = 7.4 (Figure 7A, gray and orange curves) can be explained by the relatively low protein concentration in the cell lysate compared to the prepared albumin solution leading to slower transport of hydrophobic dye through the aqueous phase. We note that although the lysate will also contain trypsin and related enzymes, which could accelerate release by providing enzymatic pathways for PCL hydrolysis, in the present experiment these pathways were blocked by the protease inhibitor cocktail. An interesting and somewhat puzzling observation is that the relative rates of decreasing nanoparticle size (Figure 7B, gray and orange curves) also suggest slightly slower PCL degradation in the cell lysate compared to the albumin solution, despite the two aqueous media being at the same temperature and pH. Although this could suggest a catalytic role of albumin in PCL degradation at physiological temperature, we note that the difference in the rates of size decrease is small compared to experimental error and further investigation is required to confirm this effect.

CONCLUSIONS

Previous work in our group has demonstrated that two-phase gas-liquid segmented microfluidic reactors enable the multiscale structure of block copolymer nanoparticles, along with their loading and release of small cargo molecules, to be controlled via the experimental handle of flow rate.[20,27-30] Here, we expanded our understanding of the complex interplay of 1. water content and 2. flow rate in this microfluidic manufacturing platform using the fluorescent dye DiI as a general surrogate for hydrophobic drug molecules. We studied the effects of these two variables on the nanoparticle morphology, size, internal crystallinity, dye loading and dye release. With respect to water content, we showed that microfluidic preparations at higher water content resulted in nanoparticles with higher core crystallinities, lower loading efficiencies, and slower release of hydrophobic cargo. With respect to flow rate, we showed that increasing flow rate resulted in higher core crystallinity at both water contents, whereas loading efficiencies and release rates showed flow dependencies dependent on the water content; at the lower water content, increasing flow rate increased loading efficiency and decreased release rate whereas at the higher water content, increasing flow rate decreased and then increased both loading efficiency and release rate. These results highlight a complex combination of thermodynamic and kinetic factors within this system. To our knowledge, this platform represents the only microfluidic reactor demonstrating flow-variability of multiscale structure and function of polymeric nanoparticles.[62-68] Therefore, the trends discovered here should inform the microfluidic manufacturing of polymeric drug delivery nanoparticles with improved structural control and efficacy.

In addition, we used a single DiI-loaded PCL-*b*-PEO nanoparticle formulation to determine the effects of the chemical and physical characteristics of the release medium on the kinetics of dye release and nanoparticle degradation. Although subtle differences in release kinetics were observed depending on temperature, pH, and the presence of albumin or cell lysate, the most important factor appeared to be the presence (or absence) of ions in the aqueous reservoir, with release into deionized water being markedly slower than other experiments. Such *in vitro* release experiments are ubiquitous in the literature,[19,20,29,32-34,36] and often employ release media with different chemical and physical properties; therefore, this study highlights that meaningful comparison of such data from different groups requires careful consideration of differences in the release media.

AUTHOR INFORMATION

Corresponding Author

mmoffitt@uvic.ca

ACKNOWLEDGMENT

We are grateful to NSERC Canada for financial support and to Drs. Alex Leung (University of Victoria), David Sinton (University of Toronto), Jason Riordon (University of Toronto) and Thomas Redelmeier (Northern Lipids Incorporated) for their respective contributions. We also acknowledge Dr. Patrick Nahirney and the UVic EM lab (Department of Biology) for the continued use of their TEM.

SUPPORTING INFORMATION

DiI fluorescence data and calibration curve; Critical water concentration determination; Representative XRD data; Additional TEM images; DiI loading efficiency data at additional flow rates; Table of actual flow rates.

REFERENCES

(1) Kataoka, K.; Harada, A.; Nagasaki, Y. Block Copolymer Micelles for Drug Delivery: Design, Characterization and Biological Significance. *Adv. Drug Deliv. Rev.* **2001**, *47*, 113-131.
(2) O'Reilly, R. K.; Hawker, C. J.; Wooley, K. L. Cross-Linked Block Copolymer Micelles: Functional Nanostructures of Great Potential and Versatility. *Chem. Soc. Rev.* **2006**, *35*, 1068-1083.
(3) Sutton, D.; Nasongkla, N.; Blanco, E.; Gao, J. M. Functionalized Micellar Systems for Cancer Targeted Drug Delivery. *Pharm. Res.* **2007**, *24*, 1029-1046.
(4) Elsabahy, M.; Wooley, K. L. Design of Polymeric Nanoparticles for Biomedical Delivery Applications. *Chem. Soc. Rev.* **2012**, *41*, 2545-2561.
(5) Zhang, L. Eisenberg, A. Multiple Morphologies of "Crew-Cut" Aggregates of Polystyrene-*b*-Poly(acrylic acid) Block Copolymers. *Science* **1995**, *268*, 1728-1731.
(6) Zhang, L. Eisenberg, A. Multiple Morphologies and Characteristics of "Crew-Cut" Micelle-like Aggregates of Polystyrene-*b*-Poly(acrylic acid) Diblock Copolymers in Aqueous Solutions *J. Am. Chem. Soc.* 1996, *118*, 3168-3181.
(7) Discher, B. M.; Won, Y.-Y.; Ege, D. S.; Lee, J. C.-M.; Bates, F. S.; Discher, D. E.; Hammer, D. A. Polymersomes: Tough Vesicles Made from Diblock Copolymers. *Science* **1999**, *284*, 1143-1146.
(8) Förster, S.; Plantenberg, T. From Self-Organizing Polymers to Nanohybrid and Biomaterials. *Angew. Chem. Int. Ed.* **2002**, *41*, 688-714.
(9) Jain, S.; Bates, F. S. On the Origins of Morphological Complexity in Block Copolymer Surfactants. *Science* **2003**, *300*, 460-464.
(10) Cui, H.; Chen, Z.; Zhong, S.; Wooley, K. L.; Pochan, D. J. Block Copolymer Assembly via Kinetic Control. *Science* **2007**, *317*, 647-650.
(11) Wang, X.; Guerin, G.; Wang, H.; Wang, Y.; Manners, I.; Winnik, M. A. Cylindrical Block Copolymer Micelles and Co-Micelles of Controlled Length and Architecture. *Science* **2007**, *317*, 644-647.
(12) Liggins, R. T.; Burt, H. M. Paclitaxel Loaded Poly(L-lactic acid) Microspheres: Properties of Microspheres Made With Low Molecular Weight Polymers. *Int. J. Pharm.* **2001**, *222*, 19-33.
(13) Liggins, R. T.; Burt, H. M. Paclitaxel Loaded Poly(L-lactic acid) (PLLA) Microspheres: II. The Effect of Processing Parameters on Microsphere Morphology and Drug Release Kinetics. *Int. J. Pharm.* **2004**, *281*, 103-106.
(14) Yang, X. Q.; Zhu, B.; Dong, T. A.; Pan, P. J.; Shuai, X. T.; Inoue, Y. S. Interactions Between an Anticancer Drug and Polymeric Micelles Based on Biodegradable Polyesters. *Macromol. Biosci.* **2008**, *8*, 1116-1125.
(15) He, W.-N.; Xu, J.-T. Crystallization Assisted Self-assembly of Semicrystalline Block Copolymers. *Prog. Polym. Sci.* **2012**, *37*, 1350-1400.
(16) Geng, Y.; Discher, D. E. Hydrolytic Degradation of Poly(ethylene oxide)-*block*-Polycaprolactone Worm Micelles. *J. Am. Chem. Soc.* **2005**, *127*, 12780-12781.
(17) Discher, D. E.; Ortiz, V.; Srinivas, G.; Klein, M. L.; Kim, Y.; Christian, D.; Cai, S.; Photos, P.; Ahmed, F. Emerging Applications of Polymersomes in Delivery: From Molecular Dynamics to Shrinkage of Tumors. *Prog. Polym. Sci.* **2007**, *32*, 838-857.
(18) Letchford, K.; Burt, H. A Review of the Formation and Classification of Amphiphilic Block Copolymer Nanoparticulate Structures: Micelles, Nanospheres, Nanocapsules and Polymersomes. *Eur. J. Pharm. Biopharm.* **2007**, *65*, 259-269.
(19) Letchford, K.; Liggins, R.; Wasan, K. M.; Burt, H. In Vitro Human Plasma Distribution of Nanoparticulate Paclitaxel is Dependent on the Physicochemical Properties of Poly(ethylene glycol)-*block*-Poly(caprolactone) Nanoparticles. *Eur. J. Pharm. Biopharm.* **2009**, *71*, 196-206.
(20) Bains, A.; Cao, Y.; Moffitt, M. G. Multiscale Control of Hierarchical Structure in Crystalline Block Copolymer Nanoparticles Using Microfluidics. *Macromol. Rapid Commun.* **2015**, DOI: 10.1002/marc.201500359
(21) Cai, S.; Vijayan, K.; Cheng, D.; Lima, E.; Discher, D. Micelles of Different Morphologies—Advantages of Worm-like Filomicelles of PEO-PCL in Paclitaxel Delivery. *Pharm. Res.* **2007**, *24*, 2099-2109.
(22) Geng, Y.; Dalhaimer, P.; Cai, S.; Tsai, R.; Tewari, M.; Minko, T.; Discher, D. E. Shape Effects of Filaments Versus Spherical Particles in Flow and Drug Delivery. *Nat Nano* **2007**, *2*, 249-255.
(23) Venkataraman, S.; Hedrick, J. L.; Ong, Z. Y.; Yang, C.; Ee, P. L. R.; Hammond, P. T.; Yang, Y. Y. The Effects of Polymeric Nanostructure Shape on Drug Delivery. *Adv. Drug Deliv. Rev.* **2011**, *63*, 1228-1246.
(24) Glover, A. L.; Nikles, S. M.; Nikles, J. A.; Brazel, C. S.; Nikles, D. E. Polymer Micelles with Crystalline Cores for Thermally Triggered Release. *Langmuir* **2012**, *28*, 10653-10660.
(25) Oltra, N. S.; Swift, J.; Mahmud, A.; Rajagopal, K.; Loverde, S. M.; Discher, D. E. Filomicelles in Nanomedicine - From Flexible, Fragmentable, and Ligand-Targetable Drug Carrier Designs to Combination Therapy for Brain Tumors. *J. Mater. Chem. B.* **2013**, *1*, 5177-5185.
(26) Fang, J.; Nakamura, H.; Maeda, H. The EPR effect: Unique Features of Tumor Blood Vessels for Drug Delivery, Factors Involved, and Limitations and Augmentation of the Effect. *Adv. Drug Deliv. Rev.* **2011**, *63*, 136-151.
(27) Wang, C.-W.; Sinton, D.; Moffitt, M. G. Flow-Directed Block Copolymer Micelle Morphologies via Microfluidic Self-Assembly. *J. Am. Chem. Soc.* **2011**, *133*, 18853-18864.
(28) Wang, C.-W.; Bains, A.; Sinton, D.; Moffitt, M. G. Flow-Directed Assembly of Block Copolymer Vesicles in the Lab-on-a-Chip. *Langmuir* **2012**, *28*, 15756-15761.
(29) Wang, C.-W.; Bains, A.; Sinton, D.; Moffitt, M. G. Flow-Directed Loading of Block Copolymer Micelles with Hydrophobic Probes in a Gas–Liquid Microreactor. *Langmuir* **2013**, *29*, 8385-8394.
(30) Wang, C.-W.; Sinton, D.; Moffitt, M. G. Morphological Control via Chemical and Shear Forces in Block Copolymer Self-Assembly in the Lab-on-Chip. *ACS Nano* **2013**, *7*, 1424-1436.
(31) Alexandridis, P.; Athanassiou, V.; Fukuda, S.; Hatton, T. A. Surface-Activity of Poly(ethylene oxide)-*block*-Poly(propylene oxide)-*Block*-Poly(Ethylene oxide) Copolymers. *Langmuir* **1994**, *10*, 2604-2612.
(32) Inoue, T.; Chen, G. H.; Nakamae, K.; Hoffman, A. S. An AB Block Copolymer of Oligo(methyl methacrylate) and Poly(acrylic acid) for Micellar Delivery of Hydrophobic Drugs. *J. Controlled Release* **1998**, *51*, 221-229.
(33) Allen, C.; Han, J. N.; Yu, Y. S.; Maysinger, D.; Eisenberg, A. Polycaprolactone-*b*-Poly(ethylene oxide) Copolymer Micelles as a Delivery Vehicle for Dihydrotestosterone. *J. Controlled Release* **2000**, *63*, 275-286.
(34) Soo, P. L.; Luo, L. B.; Maysinger, D.; Eisenberg, A. Incorporation and Release of Hydrophobic Probes in Biocompatible Polycaprolactone-*block*-Poly(ethylene oxide) Micelles: Implications for Drug Delivery. *Langmuir* **2002**, *18*, 9996-10004.
(35) Mahmud, A.; Lavasanifar, A. The Effect of Block Copolymer Structure on the Internalization of Polymeric Micelles by Human Breast Cancer cells. *Colloid Surf. B-Biointerfaces* **2005**, *45*, 82-89.

(36) Kim, S. Y.; Shin, I. L. G.; Lee, Y. M.; Cho, C. S.; Sung, Y. K. Methoxy Poly(ethylene glycol) and ϵ-Caprolactone Amphiphilic Block Copolymeric Micelle Containing Indomethacin.: II. Micelle Formation and Drug Release Behaviours. *J. Controlled Release* **1998**, *51*, 13-22.
(37) Teng, Y.; Morrison, M. E.; Munk, P.; Webber, S. E.; Procházka, K. Release Kinetics Studies of Aromatic Molecules into Water from Block Polymer Micelles. *Macromolecules* **1998**, *31*, 3578-3587.
(38) Liu, M.; Kono, K.; Fréchet, J. M. J. Water-Soluble Dendritic Unimolecular Micelles:: Their Potential as Drug Delivery Agents. *J. Controlled Release* **2000**, *65*, 121-131.
(39) Lavasanifar, A.; Samuel, J.; Kwon, G. S. Poly(ethylene oxide)-*block*-Poly(l-amino acid) Micelles for Drug Delivery. *Adv. Drug Deliv. Rev.* **2002**, *54*, 169-190.
(40) Cho, Y. W.; Lee, J.; Lee, S. C.; Huh, K. M.; Park, K. Hydrotropic Agents for Study of In Vitro Paclitaxel Release From Polymeric Micelles. *J. Controlled Release* **2004**, *97*, 249-257.
(41) Shuai, X.; Ai, H.; Nasongkla, N.; Kim, S.; Gao, J. Micellar Carriers Based on Block Copolymers of Poly(ε-caprolactone) and Poly(ethylene glycol) for Doxorubicin Delivery. *J. Controlled Release* **2004**, *98*, 415-426.
(42) Liu, J.; Zeng, F.; Allen, C. Influence of Serum Protein on Polycarbonate-Based Copolymer Micelles as a Delivery System for a Hydrophobic Anti-Cancer Agent. *J. Controlled Release* **2005**, *103*, 481-497.
(43) Liu, S. Q.; Tong, Y. W.; Yang, Y.-Y. Incorporation and In Vitro Release of Doxorubicin in Thermally Sensitive Micelles Made From Poly(N-isopropylacrylamide-co-N,N-dimethylacrylamide)-*b*-Poly(d,l-lactide-co-glycolide) With Varying Compositions. *Biomaterials* **2005**, *26*, 5064-5074.
(44) Zeng, F. Q.; Lee, H.; Allen, C. Epidermal Growth Factor-Conjugated Poly(ethylene glycol)-*block*-Poly(delta-valerolactone) Copolymer Micelles for Targeted Delivery of Chemotherapeutics. *Bioconjugate Chem.* **2006**, *17*, 399-409.
(45) Aliabadi, H. M.; Brocks, D. R.; Mahdipoor, P.; Lavasanifar, A. A Novel Use of an In Vitro method to Predict the In Vivo Stability of Block Copolymer Based Nano-Containers. *J. Controlled Release* **2007**, *122*, 63-70.
(46) Liu, J.; Zahedi, P.; Zeng, F.; Allen, C. Nano-Sized Assemblies of a PEG-Docetaxel Conjugate as a Formulation Strategy for Docetaxel. *J. Pharm. Sci.* **2008**, *97*, 3274-3290.
(47) Upadhyay, K. K.; Bhatt, A. N.; Mishra, A. K.; Dwarakanath, B. S.; Jain, S.; Schatz, C.; Le Meins, J. F.; Farooque, A.; Chandraiah, G.; Jain, A. K.; Misra, A.; Lecommandoux, S. The Intracellular Drug Delivery and Anti Tumor Activity of Doxorubicin Loaded Poly(gamma-benzyl L-glutamate)-*b*-Hyaluronan Polymersomes. *Biomaterials* **2010**, *31*, 2882-2892.
(48) Cheng, Y. X.; Hao, J.; Lee, L. A.; Biewer, M. C.; Wang, Q.; Stefan, M. C. Thermally Controlled Release of Anticancer Drug from Self-Assembled Gamma-Substituted Amphiphilic Poly(ε-caprolactone) Micellar Nanoparticles. *Biomacromolecules* **2012**, *13*, 2163-2173.
(49) Gong, J.; Chen, M. W.; Zheng, Y.; Wang, S. P.; Wang, Y. T. Polymeric Micelles Drug Delivery System in Oncology. *J. Controlled Release* **2012**, *159*, 312-323.
(50) Liu, Z. H.; Wang, Y. T.; Zhang, N. Micelle-Like Nanoassemblies Based on Polymer-Drug Conjugates as an Emerging Platform for Drug Delivery. *Expert Opinion on Drug Delivery* **2012**, *9*, 805-822.
(51) Zhang, X. C.; Burt, H. M.; VonHoff, D.; Dexter, D.; Mangold, G.; Degen, D.; Oktaba, A. M.; Hunter, W. L. An Investigation of the Antitumour Activity and Biodistribution of Polymeric Micellar Paclitaxel. *Cancer Chem. Pharmacol.* **1997**, *40*, 81-86.
(52) Kannan, S.; Kolhe, P.; Raykova, V.; Glibatec, M.; Kannan, R. M.; Lieh-Lai, M.; Bassett, D. Dynamics of Cellular Entry and Drug Delivery by Dendritic Polymers into Human Lung Epithelial Carcinoma Cells. *J. Biomater. Sci., Polym. Ed.* **2004**, *15*, 311-330.
(53) Sahu, A.; Bora, U.; Kasoju, N.; Goswami, P. Synthesis of Novel Biodegradable and Self-Assembling Methoxy Poly(ethylene glycol)–Palmitate Nanocarrier for Curcumin Delivery to Cancer Cells. *Acta Biomaterialia* **2008**, *4*, 1752-1761.
(54) Geng, Y. D., D.E. Visualization of Degradable Worm Micelle Breakdown in Relation to Drug Release. *Polymer* **2006**, *47*, 2519-2525.
(55) Geng, Y. D., P.; Cai, S.; Tsai, R.; Tewari, M.; Minko, T.; Discher, D.E. Shape Effects of Filaments Versus Spherical Particles in Flow and Drug Delivery. *Nat. Nanotechnol.* **2007**, *2*, 249-255.
(56) Vidal-Sanz, M.; Villegas-Pérez, M. P.; Bray, G. M.; Aguayo, A. J. Persistent Retrograde Labeling of Adult Rat Retinal Ganglion Cells With the Carbocyanine Dye DiI. *Exp. Neurol.* **1988**, *102*, 92-101.
(57) Asahara, T.; Murohara, T.; Sullivan, A.; Silver, M.; van der Zee, R.; Li, T.; Witzenbichler, B.; Schatteman, G.; Isner, J. M. Isolation of Putative Progenitor Endothelial Cells for Angiogenesis. *Science* **1997**, *275*, 964-966.
(58) Cuong, N.-V.; Li, Y.-L.; Hsieh, M.-F. Targeted Delivery of Doxorubicin to Human Breast Cancers by Folate-Decorated Star-Shaped PEG-PCL Micelle. *J. Mater. Chem.* **2012**, *22*, 1006-1020.
(59) Spector, T. Refinement Of Coomassie Blue Method Of Protein Quantitative - Simple and Linear Spectrophotometric Assay For Less-Than-Or-Equal-To 0.5 To 50 Mu-g Of Protein. *Anal. Biochem.* **1978**, *86*, 142-146.
(60) Sapan, C. V.; Lundblad, R. L.; Price, N. C. Colorimetric Protein Assay Techniques. *Biotechnol. Appl. Biochem.* **1999**, *29*, 99-108.
(61) Ahmad, Z.; Shah, A.; Siddiq, M.; Kraatz, H.-B. Polymeric Micelles as Drug Delivery Vehicles. *RSC Advances* **2014**, *4*, 17028-17038.
(62) Capretto, L.; Carugo, D.; Mazzitelli, S.; Nastruzzi, C.; Zhang, X. Microfluidic and lab-on-a-chip preparation routes for organic nanoparticles and vesicular systems for nanomedicine applications. *Adv. Drug Deliv. Rev.* **2013**, *65*, 1496-1532.Wang, W.; Zhang, M.J.; Chu, L.Y. Functional Polymeric Microparticles Engineered from Controllable Microfluidic Emulsions. *Acc. Chem. Research.*
(63) Khan, I. U.; Serra, C. A.; Anton, N.; Vandamme, T. Microfluidics: A focus on improved cancer targeted drug delivery systems. *J. Controlled Release* **2013**, *172*, 1065-1074.
(64) Shih, R.; Bardin, D.; Martz, T. D.; Sheeran, P. S.; Dayton, P. A.; Lee, A. P. Flow-focusing regimes for accelerated production of monodisperse drug-loadable microbubbles toward clinical-scale applications. *Lab Chip* **2013**, *13*, 4816-4826.
(65) Zhang, Y.; Chan, H. F.; Leong, K. W. Advanced materials and processing for drug delivery: The past and the future. *Adv. Drug Deliv. Rev.* **2013**, *65*, 104-120.
(67) Kong, F.; Zhang, X.; Hai, M. T. Microfluidics Fabrication of Monodisperse Biocompatible Phospholipid Vesicles for Encapsulation and Delivery of Hydrophilic Drug or Active Compound. *Langmuir* **2014**, *30*, 3905-3912.
(68) Lim, J.-M.; Swami, A.; Gilson, L. M.; Chopra, S.; Choi, S.; Wu, J.; Langer, R.; Karnik, R.; Farokhzad, O. C. Ultra-High Throughput Synthesis of Nanoparticles with Homogeneous Size Distribution Using a Coaxial Turbulent Jet Mixer. *ACS Nano* **2014**, *8*, 6056-6065.

Table of Contents